Fully polarimetric scattering from random rough layers under the geometric optics approximation: Geoscience applications

N. Pinel,[1,2] J. T. Johnson,[3] and C. Bourlier[1,2]

[1] Predictions of the geometric optics approximation for scattering from two rough interfaces that separate three homogeneous media (the "GO-layer" model) are examined for their implications for radar remote sensing. A previous formulation of the rough layer normalized radar cross section (NRCS) is also extended to allow calculation of the polarimetric covariance of the scattered field. Example results are presented for both bistatic and monostatic configurations, and show the influence of subsurface interfaces on scattered field properties. In particular, complete hemispherical bistatic patterns of both NRCS and polarimetric correlations are illustrated to provide insight into the impact of subsurface layers on these quantities. It is shown that the observability of sub-surface contributions in general is larger for geometries where upper interface returns are smaller (i.e. angles outside the quasi-specular return of the upper interface), and it is also shown that significant decorrelations between polarizations can occur in the presence of sub-surface layers. Variations of field properties with medium physical parameters (inner layer thickness and relative permittivity, upper and lower surface RMS slopes, radar frequency) are also shown. A problem that has received extensive previous interest (subsurface sensing in arid regions having an upper sand layer over a granite bedrock) is re-examined for remote sensing at higher frequencies, and it is shown that subsurface contributions can impact backscattered NRCS returns even up to X-band frequencies. The examples presented can be utilized to assess the potential detectability of sub-surface layers for both monostatic radar observations and near specular observations (as in GNSS reflection observations of land surfaces).

Citation: Pinel, N., J. T. Johnson, and C. Bourlier (2011), Fully polarimetric scattering from random rough layers under the geometric optics approximation: Geoscience applications, *Radio Sci.*, *46*, RS0E20, doi:10.1029/2010RS004621.

1. Introduction

[2] Electromagnetic wave scattering from rough layers (i.e. two rough interfaces separating three homogeneous media) has been investigated in many recent papers. While some previous studies [*Kuo and Moghaddam*, 2006; *Duan and Moghaddam*, 2010] have utilized fully numerical solutions of the boundary value problem, the computational expense for such models is high, limiting their practical application. The much lower computational expense of approximate methods makes their use desirable, so long as their inherent approximations are satisfied. Recent work developing approximate methods for the rough layer problem include *Pinel et al.* [2007, and references therein], as well

as *Kuo and Moghaddam* [2007], *Demir* [2007], *Berginc and Bourrely* [2007], and *Imperatore et al.* [2010]. The majority of these studies utilize a small perturbation solution [*Yarovoy et al.*, 2000; *Tabatabaeenejad and Moghaddam*, 2006; *Kuo and Moghaddam*, 2007; *Imperatore et al.*, 2010; M. A. Demir et al., A study of the fourth-order small perturbation method for scattering from two-layer rough surfaces, submitted to *IEEE Transactions on Geoscience and Remote Sensing*, 2011], which assumes that the heights of the interfaces are small compared to the electromagnetic wavelength. While this is most often the case of interest for radar remote sensing, since it is at low frequencies that sub-surface interfaces would be most likely to be observable, it is nevertheless of interest to develop models applicable to surfaces with roughness heights that are moderate to large in terms of the electromagnetic wavelength so that returns either at higher frequencies or for rougher surfaces at lower frequencies can be investigated.

[3] An appropriate approach for this situation is the Kirchhoff-tangent plane approximation (KA), which in conjunction with its high-frequency analytical solving method (i.e., the geometric optics approximation) was extended to predict scattering from rough layers for two-dimensional (2D) problems first [*Pinel et al.*, 2007; *Pinel and Bourlier*,

[1]Institut de Recherche en Electrotechnique et Electronique de Nantes Atlantique Laboratory, University of Nantes, Nantes, France.
[2]Now at Lunam Université - Université de Nantes, UMR CNRS 6164 Institut d'Electronique et de Télécommunications de Rennes, Nantes, France.
[3]Department of Electrical and Computer Engineering and ElectroScience Laboratory, Ohio State University, Columbus, Ohio, USA.

2008], and then extended to three-dimensional (3D) problems for flat [*Pinel et al.*, 2009] and rough [*Pinel et al.*, 2010] lower interfaces.

[4] This method obtains a mathematical expression for scattered fields by iterating the KA for each scattering at a rough interface inside the rough layer. While the initial formulation produces numerous integrals that must be evaluated numerically, the method of stationary phase (MSP) reduces the number of numerical integrations by including only specular reflection processes. A further application of the geometric optics (GO) approximation, which assumes that only closely located correlated surface points contribute to the NRCS, further reduces the computational complexity. In general the model is applicable only for surfaces with heights that are moderate to large in terms of the electromagnetic wavelength, such that the coherent component of the fields is negligible in comparison with their incoherent components.

[5] In section 2, the NRCS under the GO-layer model is reviewed, and the extension of the model to predict the polarimetric covariance of scattered fields is presented. Such an extension is motivated by interest in the potential benefits of polarimetric measurements for remote sensing, including those for near-specular bistatic measurements as in the sensing of land surfaces with Global Navigation Satellite System (GNSS) reflectivity [*Zavorotny et al.*, 2010]. Sample geoscience and remote sensing applications are presented in section 3, including examination of fully polarimetric returns in the complete hemispherical bistatic scattering pattern. It is shown that some portions of the bistatic pattern provide enhanced visibility of sub-surface returns, so that utilization of these portions may be of interest in future measurements. A renewed examination of a problem that has received extensive previous interest, the remote sensing of sub-surface properties in arid regions, is also performed in order to assess the utilization of higher microwave frequencies. Particular angular regions for monostatic observations of sub-surface properties are then determined as a function of surface roughness and layer dielectric properties.

[6] In general the results provide useful insight into the impact of sub-surface layers of radar remote sensing of land surface properties, and can be utilized in the design of future sensors for sub-surface sensing applications.

2. NRCS and Polarimetric Covariance Under the GO-Layer Model

2.1. NRCS (Normalized Radar Cross Section)

[7] In this paper, we focus on the case of a rough layer with a rough lower interface [*Pinel et al.*, 2010]. For the simple case of a 2D problem, by iterating the KA for scattering from the rough layer and by using the geometric optics (GO) approximation, the normalized radar cross section (NRCS) associated with one reflection onto the lower interface can be expressed in a very simple manner. This NRCS contribution, called the second-order NRCS and denoted $\sigma_{r,2}^{2D}$, can be expressed in terms of a product of elementary NRCSs related to each elementary scattering inside the rough layer: first, the scattering in transmission from the incidence medium Ω_1 into the rough layer Ω_2 denoted σ_{t12}^{2D}, second, the scattering in reflection inside Ω_2 onto the (rough) lower interface (and separating the lower medium Ω_3) of the

rough layer denoted σ_{r23}^{2D}, and third, the scattering in transmission from Ω_2 back into the incidence medium Ω_1 denoted σ_{t21}^{2D}. The resulting second order NRCS is expressed as (see equation (20) of *Pinel and Bourlier* [2008])

$$\sigma_{r,2}^{2D}(\mathbf{k_r}, \mathbf{k_i}) = \frac{1}{\cos\theta_i}\int d\theta_{m1}d\theta_{p1}\sigma_{t12}^{2D}(\mathbf{k_{m1}}, \mathbf{k_i}) \cdot \sigma_{r23}^{2D}(\mathbf{k_{p1}}, \mathbf{k_{m1}})\sigma_{t21}^{2D}(\mathbf{k_r}, \mathbf{k_{p1}}), \quad (1)$$

with θ_{m1} the propagation angle of the wave after transmission from Ω_1 into the layer Ω_2, and θ_{p1} the angle inside Ω_2 after reflection from the lower interface. Each elementary NRCS $\sigma_{s\alpha\beta}(\mathbf{k}_\beta, \mathbf{k}_\alpha)$ (with $s \equiv r$ and $s \equiv t$ for scattering in reflection and in transmission, respectively) can be expressed as the product of three terms: a projection and polarization term for given incidence and scattering wave vectors $\mathbf{k}_\alpha$ and $\mathbf{k}_\beta$, $f_{s\alpha\beta}(\mathbf{k}_\beta, \mathbf{k}_\alpha)$, the considered surface slope PDF (probability density function) evaluated at surface points of stationary phase $\gamma_M = \gamma_M^{0(s)}$, $p_s(\gamma_M^{0(s)})$, and the surface shadowing function $S_{\alpha\beta}(\mathbf{k}_\beta, \mathbf{k}_\alpha)$ [*Pinel and Bourlier*, 2008]:

$$\sigma_{s\alpha\beta}^{2D}(\mathbf{k}_\beta, \mathbf{k}_\alpha) = \left|f_{s\alpha\beta}(\mathbf{k}_\beta, \mathbf{k}_\alpha)\right|^2 \frac{p_s\left(\gamma_M^{0(s)}\right)}{\left|\hat{k}_{\beta z} - \frac{k_\alpha}{k_\beta}\hat{k}_{\alpha z}\right|^2} S_{\alpha\beta}\left(\mathbf{k}_\alpha, \mathbf{k}_\beta\big|\gamma_M^{0(s)}\right), \quad (2)$$

with $\hat{k}_{\alpha z}$ and $\hat{k}_{\beta z}$ the projection of the normalized wave vector $\hat{\mathbf{k}}_\alpha$ and $\hat{\mathbf{k}}_\beta$ onto the vertical axis $\hat{\mathbf{z}}$, respectively.

[8] In the 3D case, the principle is exactly the same as for the more simple 2D case, and the elementary NRCS can be expressed as:

$$\bar{\sigma}_{s\alpha\beta}(\mathbf{K}_\beta, \mathbf{K}_\alpha) = \left|\bar{F}_{s\alpha\beta}(\mathbf{K}_\beta, \mathbf{K}_\alpha)\right|^2 \frac{p_s\left(\gamma_\mathbf{M}^{0(\mathbf{s})}\right)}{\left|\hat{k}_{\beta z} - \frac{k_\alpha}{k_\beta}\hat{k}_{\alpha z}\right|^2} S_{\alpha\beta}\left(\mathbf{K}_\alpha, \mathbf{K}_\beta\big|\gamma_\mathbf{M}^{0(\mathbf{s})}\right). \quad (3)$$

However, owing to the polarization (and physically, in order to account for cross-polarized elementary contributions), the product of the elementary polarization terms $\bar{F}_{s\alpha\beta}$ is a Sinclair matrix product which cannot be simplified to a scalar product as in 2D. As a consequence, the second-order NRCS for the 3D case is written as [*Pinel et al.*, 2010]

$$\bar{\sigma}_{r,2}(\mathbf{K_r}, \mathbf{K_i}) = \int \frac{\sin\theta_{m1}}{\cos\theta_i}d\theta_{m1}d\phi_{m1}\sin\theta_{p1}d\theta_{p1}d\phi_{p1}$$

$$\left|\bar{F}_{t21}(\mathbf{K_{p1}}, \mathbf{K_r}) \times \bar{F}_{r23}(\mathbf{K_{m1}}, \mathbf{K_{p1}}) \times \bar{F}_{t12}(\mathbf{K_i}, \mathbf{K_{m1}})\right|^2$$

$$\frac{p_s\left(\gamma_{\mathbf{A_1}}^{0(\mathbf{t})}\right)}{\left|\hat{k}_{m1z} - \frac{k_1}{k_2}\hat{k}_{iz}\right|^2}S_{12}\left(\mathbf{K_i}, \mathbf{K_{m1}}\big|\gamma_{\mathbf{A_1}}^{0(\mathbf{t})}\right)$$

$$\frac{p_s\left(\gamma_{\mathbf{B_1}}^{0(\mathbf{r})}\right)}{\left|\hat{k}_{p1z} - \hat{k}_{m1z}\right|^2}S_{22}\left(\mathbf{K_{m1}}, \mathbf{K_{p1}}\big|\gamma_{\mathbf{B_1}}^{0(\mathbf{r})}\right)$$

$$\frac{p_s\left(\gamma_{\mathbf{A_2}}^{0(\mathbf{t})}\right)}{\left|\hat{k}_{rz} - \frac{k_2}{k_1}\hat{k}_{p1z}\right|^2}S_{21}\left(\mathbf{K_{p1}}, \mathbf{K_r}\big|\gamma_{\mathbf{A_2}}^{0(\mathbf{t})}\right). \quad (4)$$

[9] The model validity domain was thoroughly studied in previous works [*Pinel and Bourlier*, 2008; *Pinel et al.*, 2010]. In short, the GO-layer model is able to compute the NRCS of homogeneous rough layers having surfaces of

gentle slopes (RMS slopes less than $0.3 - 0.4$, approximately) and moderate to large heights such that the nth-order NRCS contribution satisfies the Rayleigh roughness criterion $Ra_{r,n} \gtrsim \pi/2$ (see section 2.C of *Pinel and Bourlier* [2008]). Because the model does not take multiple scattering at a single interface into account, the GO-layer model underestimates the NRCS when it is small (less than the order of -30 dB). Such situations include cross-polarized scattering in the plane of incidence [*Pinel et al.*, 2010].

[10] In what follows, the GO-layer model for the NRCS is extended to the prediction of polarimetric covariances.

2.2. Covariance of the Scattered Field

[11] The preceding expressions for the NRCS quantities $\bar\sigma_{r,1}$ and $\bar\sigma_{r,2}$ can be extended for calculating the covariance between fields in two polarizations, pq and rs, with $\{p; q; r; s\} = \{V; H\}$. For a single rough surface, this expression is

$$\sigma^{pq(rs)*}{}_{s\alpha\beta}(\mathbf{K}_\beta, \mathbf{K}_\alpha) = F^{pq}_{s\alpha\beta}(\mathbf{K}_\beta, \mathbf{K}_\alpha) F^{rs\,*}_{s\alpha\beta}(\mathbf{K}_\beta, \mathbf{K}_\alpha)$$
$$\cdot \frac{p_s\left(\gamma^{0(\mathbf{s})}_{\mathbf{M}}\right)}{\left|\hat{k}_{\beta z} - \frac{k_\alpha}{k_\beta}\hat{k}_{\alpha z}\right|^2} S_{\alpha\beta}\left(\mathbf{K}_\alpha, \mathbf{K}_\beta \big| \gamma^{0(\mathbf{s})}_{\mathbf{M}}\right). \quad (5)$$

Then, the extension to the scattering from a rough layer can easily be understood to be

$$\sigma^{pq(rs)*}_{r,2}(\mathbf{K_r}, \mathbf{K_i}) = \int d\theta_{m1} d\phi_{m1} d\theta_{p1} d\phi_{p1} \frac{\sin\theta_{m1}}{\cos\theta_i}\sin\theta_{p1}$$
$$\left[\bar{F}_{t21}(\mathbf{K_{p1}}, \mathbf{K_r}) \times \bar{F}_{r23}(\mathbf{K_{m1}}, \mathbf{K_{p1}}) \times \bar{F}_{t12}(\mathbf{K_i}, \mathbf{K_{m1}})\right]^{pq}$$
$$\left[\bar{F}_{t21}(\mathbf{K_{p1}}, \mathbf{K_r}) \times \bar{F}_{r23}(\mathbf{K_{m1}}, \mathbf{K_{p1}}) \times \bar{F}_{t12}(\mathbf{K_i}, \mathbf{K_{m1}})\right]^{*,rs}$$
$$\frac{p_s\left(\gamma^{0(\mathbf{t})}_{\mathbf{A_1}}\right)}{\left|\hat{k}_{m1z} - \frac{k_1}{k_2}\hat{k}_{iz}\right|^2} S_{12}\left(\mathbf{K_i}, \mathbf{K_{m1}} \big| \gamma^{0(\mathbf{t})}_{\mathbf{A_1}}\right)$$
$$\frac{p_s\left(\gamma^{0(\mathbf{r})}_{\mathbf{B_1}}\right)}{\left|\hat{k}_{p1z} - \hat{k}_{m1z}\right|^2} S_{22}\left(\mathbf{K_{m1}}, \mathbf{K_{p1}} \big| \gamma^{0(\mathbf{r})}_{\mathbf{B_1}}\right)$$
$$\frac{p_s\left(\gamma^{0(\mathbf{t})}_{\mathbf{A_2}}\right)}{\left|\hat{k}_{rz} - \frac{k_2}{k_1}\hat{k}_{p1z}\right|^2} S_{21}\left(\mathbf{K_{p1}}, \mathbf{K_r} \big| \gamma^{0(\mathbf{t})}_{\mathbf{A_2}}\right). \quad (6)$$

The total covariance is obtained by summing the two terms (i.e. the upper surface return and the upper-lower surface interaction term) in the series. The correlation is expressed from the covariance through the relation $\rho^{pq(rs)*}_{r,n} = \sigma^{pq(rs)*}_{r,n}/\sqrt{\sigma^{pq}_{r,n}\sigma^{rs}_{r,n}}$.

[12] In what follows, the GO-layer model is used in sample geoscience applications, for both bistatic and monostatic configurations.

3. Numerical Results of the GO-Layer Model

[13] Numerical results are presented for three configurations: sensing of (dry) sand over granite [*Elachi et al.*, 1984; *Saillard and Toso*, 1997] at X-band, subsurface sensing of hyper-saline soil [*Shao et al.*, 2009; *Gong et al.*, 2009a], and soil moisture impacts on monostatic returns from clay under (dry) sand [*Kuo and Moghaddam*, 2007; *Moghaddam et al.*, 2007; *Kuo*, 2008]. Rough surface profiles are assumed to be isotropic stationary Gaussian random processes, and to have a Gaussian height autocorrelation function; these properties

result additionally in a Gaussian distribution of surface slopes. The two surface profiles of the rough layer are assumed to be statistically independent.

3.1. Sub-surface Sensing in Arid Regions: Bistatic Case

[14] The first study case considers the sensing of sand over granite at X-band ($f = 10$ GHz) in a configuration used in former studies at lower frequencies [*Elachi et al.*, 1984; *Saillard and Toso*, 1997]. Previous studies have shown that sub-surface returns are observable in such cases due to the relatively low attenuation in the dry sand layer. However, the impact of larger surface roughnesses relative to the wavelength (i.e. higher radar frequencies) has not been considered due to limitations of the models previously utilized. Complete bistatic patterns are examined in this section to determine any potential advantages in the use of bistatic observations for observing sub-surface layer properties.

[15] The references have shown that the RMS height of the upper surface σ_{hA} is on the order of 1 centimeter and the correlation length $L_{cAx} = L_{cAy} \equiv L_{cA}$ of this surface is on the order of a few tens of centimeters [*Grandjean et al.*, 2001; *Kuo and Moghaddam*, 2007; *Moghaddam et al.*, 2007; *Kuo*, 2008]. We select $\sigma_{hA} = 1.5$ cm and $L_{cA} = 20$ cm, so that the RMS slope is $\sigma_{sA} \simeq 0.106$. The lower granite surface is rougher with an RMS height of a few centimeters [*Saillard and Toso*, 1997]; we select $\sigma_{hB} = 5.0$ cm and $L_{cBx} = L_{cBy} \equiv L_{cB} = 20$ cm, so that the RMS slope $\sigma_{sB} \simeq 0.354$. The use of X-band with these surface parameters ensures the validity of the GO-layer model since the Rayleigh roughness criterion is satisfied.

[16] The upper surface layer is modeled as dry sand with relative permittivity $\epsilon_{r2} = 3.3 + 0.01i$ [*Saillard and Toso*, 1997; *Fuks*, 1998; *Sarabandi and Chiu*, 1997], while the lower granite medium is modeled with $\epsilon_{r3} = 7 + 0.1i$ [*Saillard and Toso*, 1997; *Prigent et al.*, 2005]. The skin depth in the sand $d = 1/(k_0 n''_2)$ (with k_0 the wave number in vacuum and $n''_2 = \text{Im}\sqrt{\epsilon r_2}$ the imaginary part of the refraction index of the sand) is equal to $d \simeq 173$ cm. In the results to follow, we will consider variations of the mean layer thickness $\bar{H}$ by taking $\bar{H} = \{10; 50; 100; 150\}$ cm.

[17] First we consider in-plane bistatic scattering (i.e., azimuth angle $\phi_r - \phi_i = 0°$) for an incidence angle $\theta_i = 40°$ in HH, VV, HV, and VH NRCS returns. Figure 1 plots the first- and second-order total NRCS, $\sigma^{tot}_{r,1} = \sigma_{r,1}$ and $\sigma^{tot}_{r,2} = \sigma_{r,1} + \sigma_{r,2}$, respectively, as the sand layer thickness is varied over $\bar{H} = \{10; 50; 100; 150\}$ cm. As a reminder, $\sigma_{r,1}$ corresponds to the scattering from the upper sand interface only, neglecting the presence of the granite medium. For co-polarized returns, the presence of the subsurface layer has negligible impact for forward scattering regions, but a significant impact for observation angles $\theta_r \lesssim 0$. In particular, it can be seen that in backscattering $\theta_r = -40°$, the impact of the lower granite medium on the scattering process is strong. Larger layer thicknesses $\bar{H}$ cause smaller second-order contributions $\sigma_{r,2}$ due to the increased attenuation of lower medium returns (or in other words, due to increased propagation losses inside the inner sand layer), so that the granite medium is observable only at larger negative bistatic scattering angles. The plots show negligible cross-polarized returns due to the neglect of multiple scattering at a single interface.
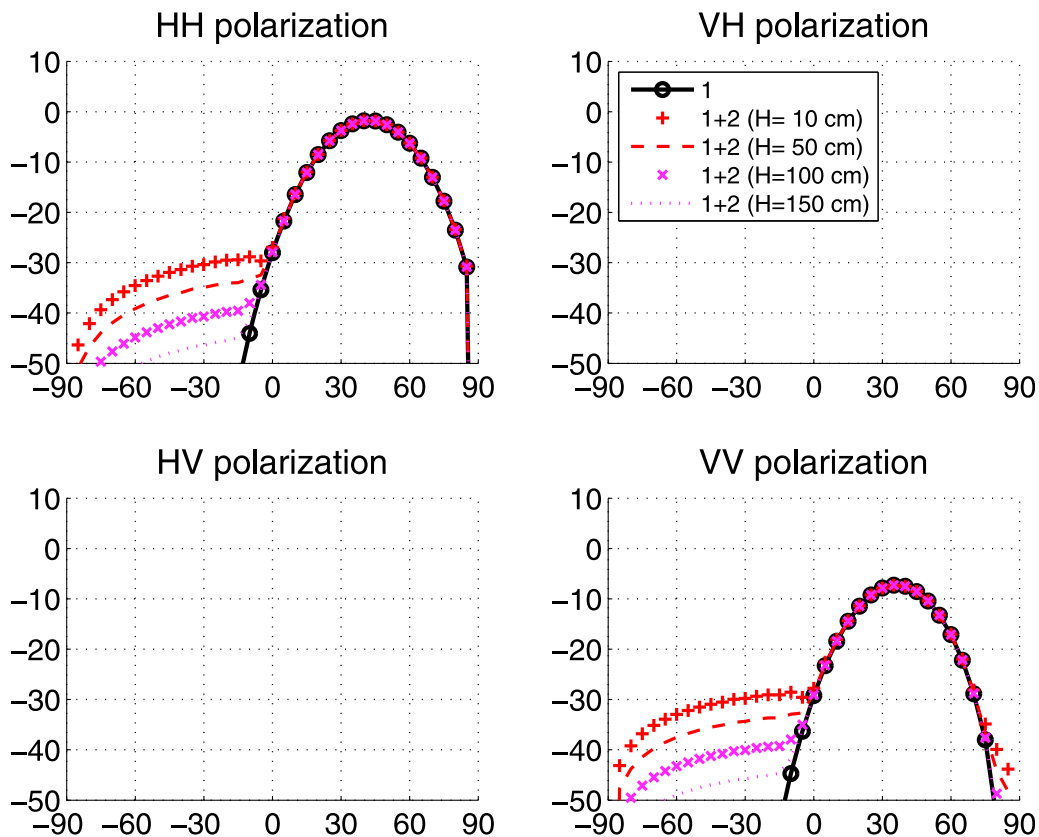
Figure 1. First two total NRCSs $\sigma_{r,1}^{tot}$, and $\sigma_{r,2}^{tot}$ (dB) of dry sand over granite at X-band with respect to the observation polar angle θ_r in the plane of incidence (i.e., azimuth angle $\phi_r - \phi_i = 0°$), for an incident polar angle $\theta_i = 40°$.

[18] Figure 2 presents the same simulations as in Figure 1, but for scattering outside the plane of incidence (azimuth angle $\phi_r - \phi_i = 75°$). In this configuration, reduced co-pol and increased cross-pol NRCS levels are observed. Here the first-order co-pol NRCS $\sigma_{r,1}$ is significant only for $\theta_r \in$ [−5°; 10°] approximately, and is otherwise negligible compared to $\sigma_{r,2}$. This configuration emphasizes that subsurface detection for moderate to large roughness surfaces may be improved by choosing observation geometries such that first-order scattering from the upper interface is reduced. A choice of observations in the vicinity of, but not at, the specular direction, as is possible in GNSS reflection measurements, may be useful in sensing subsurface layer properties.

[19] Figure 3 presents complete bistatic plots of the first-order NRCS $\sigma_{r,1}$ (left), second-order NRCS $\sigma_{r,2}$ (middle), and second-order total NRCS $\sigma_{r,2}^{tot} = \sigma_{r,1} + \sigma_{r,2}$ (right) for the same simulation parameters as in Figure 1, except for the layer thickness $\bar{H} = 30$ cm and for horizontal (H) incidence only. The specular direction is marked by a plus sign, and the backscattering direction by a circle. Figure 4 plots the same simulations as in Figure 3, but for vertical (V) incidence. For the first-order NRCS $\sigma_{r,1}$ on the left of the two figures, which corresponds to scattering from the upper sand surface only, it can be seen that the scattered energy concentrates around the specular direction for both co- and cross-polarizations. Moreover, HH co-polarization has a slightly higher and more spread NRCS than VV co-polarization, while HV and VH cross-polarizations show more similar

features. For the second-order NRCS $\sigma_{r,2}$ in the middle of the two figures, the scattered energy is spread over a large range of angles for both co- and cross- polarizations, with levels between −40 and −30 dB, approximately. For co-polarizations, $\sigma_{r,2}$ contributes for moderate observation angles θ_r away from the orthogonal azimuthal direction $\phi_r - \phi_i = 90°$, whereas for cross-polarizations, it is the reverse: $\sigma_{r,2}$ contributes for moderate θ_r away from the plane of incidence $\phi_r - \phi_i = 0°$. The total second-order NRCS $\sigma_{r,2}^{tot}$ clearly highlights differences with the simple case of a single dry sand interface $\sigma_{r,1}$. Indeed, even if the second-order contribution $\sigma_{r,2}$ is negligible around the specular direction where the first-order one $\sigma_{r,1}$ is significant, clear differences appear away from the specular direction. In particular, significant differences appear away from the backscattering direction for cross-polarizations and around the backscattering direction for co-polarizations. In general, these plots make clear the strong impact of the lower medium on scattering, and in particular on (and around) backscattering for co-polarizations.

3.2. Sub-surface Sensing in Arid Regions: Correlation Full Bistatic Plots

[20] Correlation behaviors (in both amplitude and phase) are also of interest in polarimetric remote sensing. Note that for the first-order correlation $\rho_{r,1}$, the correlation amplitude is always equal to 1. This is not surprising, because looking at equation (5), it can be seen that the relation between
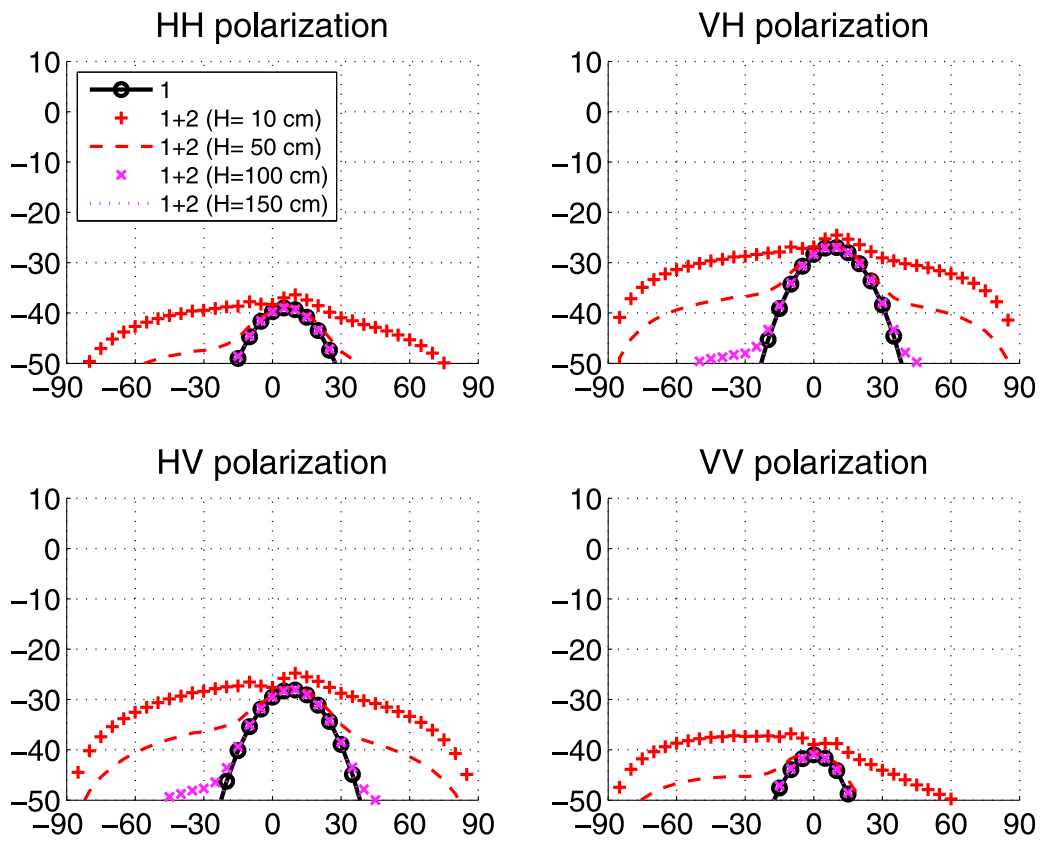
Figure 2. Same simulations as in Figure 1, but for an azimuth angle $\phi_r - \phi_i = 75°$.
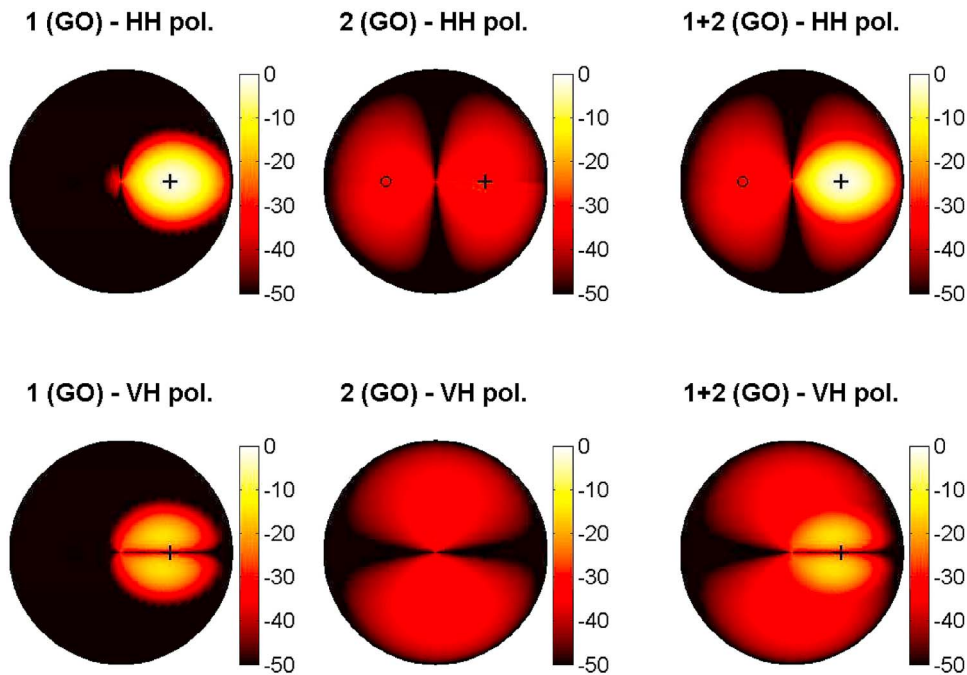

Figure 3. H incidence full bistatic plot of (left) first-order NRCS $\sigma_{r,1}$, (middle) second-order NRCS $\sigma_{r,2}$, and (right) second-order total NRCS $\sigma_{r,2}^{tot} = \sigma_{r,1} + \sigma_{r,2}$, of dry sand layer of thickness $\bar{H} = 30$ cm (over granite) at X-band (with respect to the observation elevation angle θ_r and to the azimuth angle $\phi_r - \phi_i = 0°$), for an incidence elevation angle $\theta_i = 40°$.

1 (GO) - VV pol. **2 (GO) - VV pol.** **1+2 (GO) - VV pol.**

1 (GO) - HV pol. **2 (GO) - HV pol.** **1+2 (GO) - HV pol.**
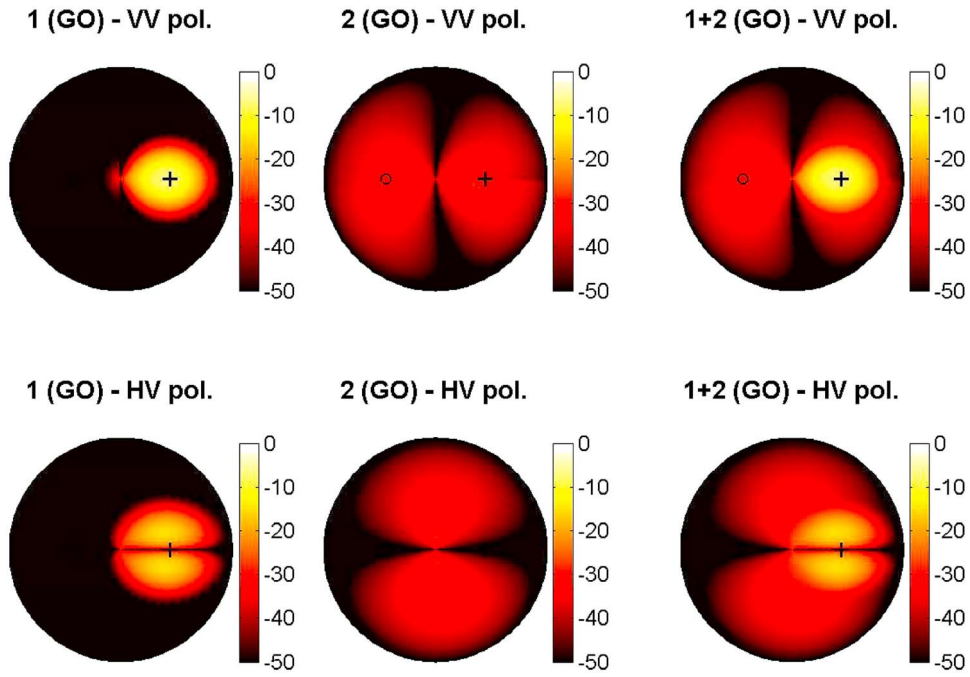
Figure 4. Same simulations as in Figure 3, but for V incidence.

two polarizations pq and rs is a constant for a given angular configuration. Then, the correlation is equal to $F_r^{pq}/|F_r^{pq}|F_r^{rs}/|F_r^{rs}|$, which has a unitary amplitude and a phase equal to $\angle F_r^{pq} - \angle F_r^{rs}$. In addition, for a low loss dielectric layer as considered here, $\angle F_r^{pq}$ and $\angle F_r^{rs}$ are very close to either 0° or 180°.

[21] Because it is typically assumed that the co-pol polarimetric correlation is near unity for surface scattering in general, any significant deviation from unity caused by subsurface layers is of particular interest. Such changes could potentially result in confusion between sub-surface and vegetation effects, as it is often expected that decreased co-pol correlations arise primarily from volume-scatter or double-bounce effects.

[22] Figure 5 presents the correlation amplitude $\left|\rho_{r,2}^{tot,pq(rs)*}\right|$ plot for the second-order total correlation $\rho_{r,2}^{tot}$. To show

1+2 - VV(HH)* pol. **1+2 - VH(HH)* pol.** **1+2 - HV(HH)* pol.**

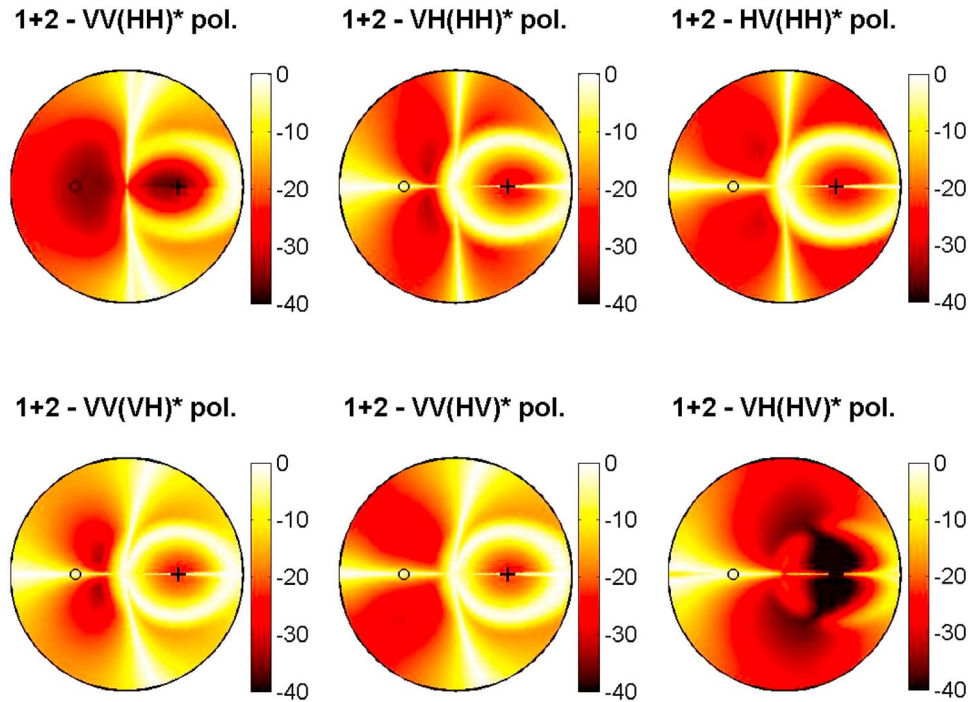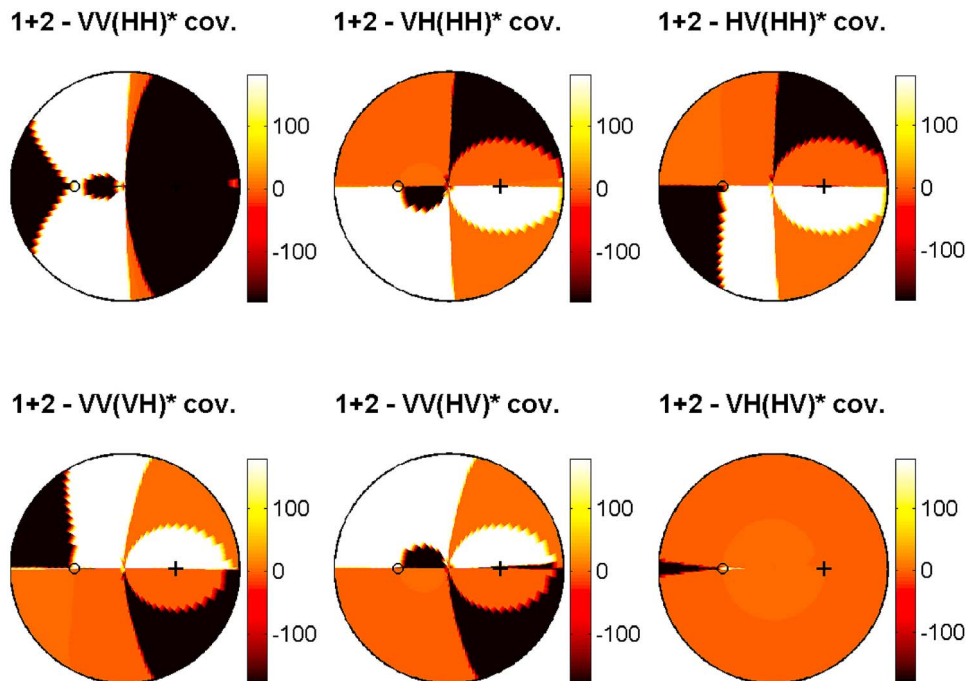**1+2 - VV(VH)* pol.** **1+2 - VV(HV)* pol.** **1+2 - VH(HV)* pol.**

Figure 5. Same simulations as in Figure 3, but for correlation amplitude plot $(1 - |\rho_{r,2}^{tot,pq(rs)*}|)$ of the second-order total NRCS $\sigma_{r,2}^{tot}$.

Figure 6. Same simulations as in Figure 3, but for correlation phase plot of the second-order total NRCS $\sigma_{r,2}^{tot}$.

correlation amplitude variations more clearly, Figure **5** plots $1 - |\rho_{r,2}^{tot,pq(rs)^*}|$ (rather than $|\rho_{r,2}^{tot,pq(rs)^*}|$) using a dB scale. It can be seen that contrary to the first-order contribution for which the correlation amplitude is always unity, significant de-correlations between polarizations can indeed be observed in some angular regions. In particular, decreased correlation amplitudes in the plane of incidence and around the orthogonal plane $\phi_r - \phi_i = 90°$ are associated with small values of the corresponding cross sections (NRCS) in these regions. However, a significant de-correlation also occurs in a region that forms a circle around the specular direction, and which corresponds to the limits of the region where the first-order NRCS significantly contributes to the scattering process (see Figures 3 and 4). In such regions, the uncorrelated returns from the upper and lower interfaces are of similar amplitudes, thereby resulting in a reduced correlation among fields.

[23] The correlation phase of the first-order contribution $\rho_{r,1}$ (not shown here) shows that, as expected, it takes values very close to either 0° or 180°. Figure 6 plots the total second-order $\rho_{r,2}^{tot}$ correlation phase, which also takes values close to either 0 or ±180°. Interestingly, an ellipse (rather than a circle) appears around the specular direction for $VH(HH)^*$, $HV(HH)^*$, $VV(VH)^*$, and $VV(HV)^*$ correlations, which is characteristic of the first-order NRCS contribution. It must be highlighted that although this ellipse does not appear in $VV(HH)^*$ correlation, it does appear in $VH(HH)^*$ and $HV(HH)^*$ correlations.

[24] The presence of significant decorrelations caused by sub-surface layers suggests the potential of these measurements for detecting the influence of sub-surface returns. Again these effects occur primarily in bistatic angles, and would be relevant for GNSS reflections sensing at angles near the specular direction.

[25] Now, let us study the influence of variations of the inner layer thickness $\bar{H}$, the sand moisture content, and the surface roughness properties (i.e., the surface RMS slopes) on the rough layer backscattering returns.

3.3. Sensing of Sand Over Granite at X-Band: Monostatic Plots

[26] Co-pol backscattering returns from the rough layer are investigated in this section. Cross-pol is not considered due to the limitations of the GO-layer model (neglect of single interface multiple scattering) for in-plane cross-pol returns. Polarimetric correlations are also not considered; note that co-cross pol correlations vanish identically due to the statistical symmetry of the geometry, while the VVHH correlation is very close to unity.

[27] Figure 7 plots the same simulations as in Figure 1 for sand layer thicknesses $\bar{H} = \{10; 50; 100; 150\}$ cm, but for a monostatic configuration, with the observation elevation angle $\theta_r \in [0°; 75°]$. HH polarization is plotted, as well as the VV/HH polarization ratio in linear scale. The results show behaviors similar to the bistatic plots of Figure 1. The lower layer impacts returns from the sand surface for observation angles $\theta_r \gtrsim 25°$. Also, the results from the different layer thicknesses show significant differences between one another owing to the propagation losses inside the sand layer. Under the GO model the polarization ratio is unity for the sand surface only, while it increases from 1 to nearly 3 versus θ_r when both layers are considered.

[28] To consider the effect of varying lower surface roughness, Figure 8 plots the same simulations as in Figure 7, but by varying the lower surface RMS slope $\sigma_{sB} = \{0.1; 0.2; 0.3; 0.4\}$ for layer thickness $\bar{H} = 30$ cm. Increasing the lower surface RMS slope σ_{sB} should be expected to induce a
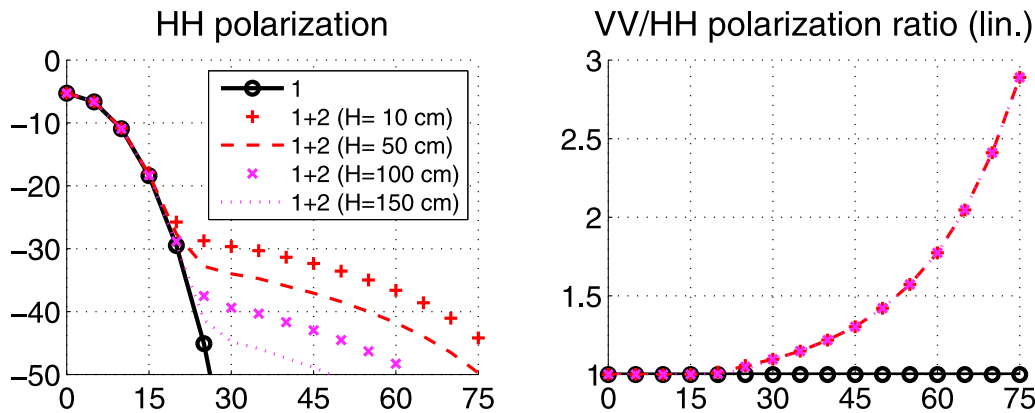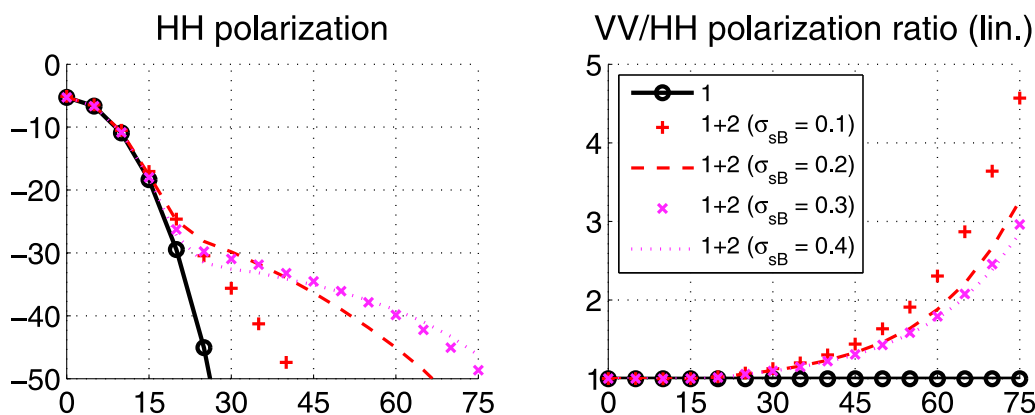
Figure 7. Same simulations as in Figure 1, but for monostatic configuration: plot of *HH* polarization and *VV/HH* polarization ratio in linear scale.

broadening of the second-order NRCS $\sigma_{r,2}$ away from the specular direction, so that close to specular levels are decreased while those far from specular are increased. As a consequence, we observe that when σ_{sB} increases, the observation angle θ_r at which $\sigma_{r,2}$ appreciably contributes to $\sigma_{r,2}^{tot}$ increases. Also, when σ_{sB} is increased, $\sigma_{r,2}^{tot}$ is correspondingly increased at larger observation angles. In addition, the polarization ratio decreases as the lower surface RMS slope σ_{sB} increases for high observation angles θ_r.

[29] For varying upper surface roughness, Figure 9 plots the same simulations as in Figure 8, but by varying the upper surface RMS slope $\sigma_{sA} = \{0.1; 0.2; 0.3\}$ for fixed $\sigma_{sB} = 0.354$. For each σ_{sA}, both the first- and second- order contributions are modified. Increasing the upper RMS slope σ_{sA} induces a broadening of $\sigma_{r,1}$ away from specular, and similarly a broadening of the total monostatic NRCS. The near nadir ($\theta_r = 0$) monostatic NRCS decreases, but the rate of decrease in $\sigma_{r,1}$ when θ_r increases is slower so that the "contributing range" of $\sigma_{r,1}$ to the total layer cross section is larger. As the second-order contribution $\sigma_{r,2}$ does not vary significantly when σ_{sA} increases, the observation angle at which the subsurface layer contribution is significant increases with σ_{sA}: for $\sigma_{sA} = 0.1$, it is equal to $\theta_r \gtrsim 15°$, for $\sigma_{sA} = 0.2$, it is equal to $\theta_r \gtrsim 30°$, and for $\sigma_{sA} = 0.3$, it is equal

to $\theta_r \gtrsim 45°$. It is again observed that the polarization ratio decreases as the upper surface RMS slope σ_{sA} increases for high observation angles θ_r.

[30] The influence of the sand layer moisture is studied in Figure 10, which compares results for sand relative permittivities $\epsilon_{r2} = \{3.3 + 0.01i; 5.0 + 0.01i; 5.0 + 0.1i\}$. The mean layer thickness remains $\bar{H} = 30$ cm, which must be compared with the skin depth $d = 1/(k_0 n_2'')$, which for the three cases is $d = \{173; 214; 21\}$ cm, respectively. First, by comparing the first two cases $3.3 + 0.01i$ and $5.0 + 0.01i$, it can be seen that increasing the real part of ϵ_{r2} slightly increases the first-order NRCS $\sigma_{r,1}$ and significantly decreases the second-order NRCS $\sigma_{r,2}$ due to the increased reflection from and reduced transmission into the sand layer. Second, by comparing the two cases $5.0 + 0.01i$ and $5.0 + 0.1i$, it can be seen that observable differences occur only for the second-order NRCS $\sigma_{r,2}$. Indeed, as both cases are cases of low losses, the first-order NRCS $\sigma_{r,1}$ is not significantly modified by increasing the imaginary part of ϵ_{r2}. By contrast, for $\sigma_{r,2}$, the larger propagation losses inside the sand for the $5.0 + 0.1i$ case results in a negligible second-order contribution to the total cross section. These results provide examples of the importance of both dielectric contrast and attenuation in observing subsurface layers, and provide useful information

Figure 8. Same simulations as in Figure 7, but for various lower surface RMS slope $\sigma_{sB} = \{0.1; 0.2; 0.3; 0.4\}$ with a constant layer thickness $\bar{H} = 30$ cm.
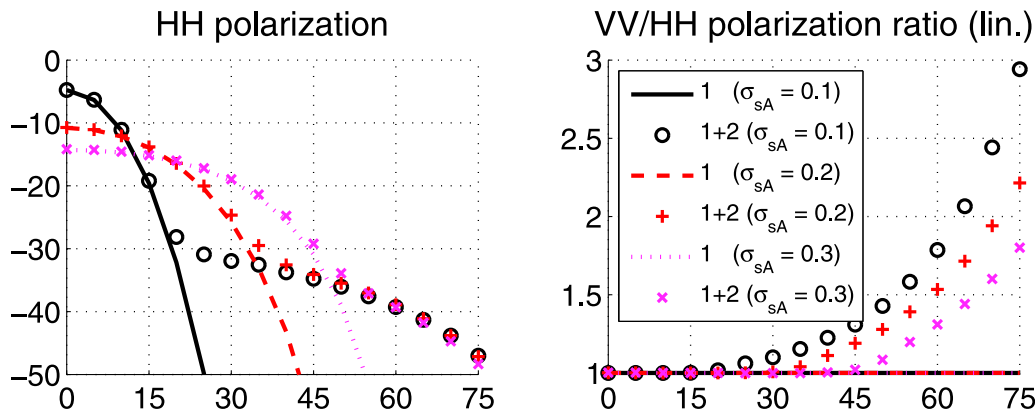
Figure 9. Same simulations as in Figure 7, but for various upper surface RMS slope $\sigma_{sA} = \{0.1; 0.2; 0.3\}$ with a constant layer thickness $\bar{H} = 30$ cm.

for interpreting the remote sensing of sub-surface layers in arid regions, in particular with regard to the visibility of sub-surface regions.

3.4. Subsurface Sensing of Hyper-saline Soil: Monostatic Case

[31] An additional case is considered that corresponds to a study from Lop Nur lake involving a sand layer overlying clay that is hyper-saline [*Shao et al.*, 2009; *Gong et al.*, 2009a, 2009b]. Using serial number 1 in the work of *Gong et al.* [2009a, 2009b], the sand layer has $\epsilon_{r2} = 4.43 + 0.01i$ and mean thickness $\bar{H} = 35$ cm, while the clay lower medium has $\epsilon_{r3} = 19.94 + 71.58i$. The upper surface has RMS height $\sigma_{hA} = 7.00$ cm and correlation length $L_{cA} = 50.00$ cm, which implies an RMS slope $\sigma_{sA} \simeq 0.198$ under an assumption of Gaussian surface statistics. The lower surface has RMS height $\sigma_{hB} = 0.40$ cm and correlation length $L_{cB} = 6.10$ cm, which implies an RMS slope $\sigma_{sB} \simeq 0.093$.

[32] First, three bands are studied in Figure 11: L-band ($f = 1.27$ GHz), C-band ($f = 5.3$ GHz), and X-band ($f = 10$ GHz). Note that it has been checked that the GO-layer model is applicable for all chosen frequencies.

[33] The results show that in this case the total second-order NRCS $\sigma_{r,2}^{tot}$ is always larger than the first-order $\sigma_{r,1}$. These differences from the earlier case considered arise from the difference of contrast in relative permittivities: here, the

contrast is higher, making the second-order NRCS contribution $\sigma_{r,2}$ larger. This is further reinforced by the small lower surface RMS slope σ_{sB}. Comparing the results for the three frequencies, as expected there is no impact on $\sigma_{r,1}$. Also, the impact on $\sigma_{r,2}$ is low: by varying the frequency with other parameters kept constant, the only modification in the GO-layer model comes from the propagation losses inside the inner sand layer. For $f = \{1.27; 5.3; 10\}$ GHz, the skin depth $d = \{15.8; 3.8; 2.0\}$ m is significantly larger than the inner layer thickness $\bar{H} = 35$ cm, so that $\sigma_{r,2}^{tot}$ does not vary significantly with f. In fact, increasing the frequency is similar to increasing the layer thickness, so that the same qualitative observations can be made here as for Figure 1. As a check, numerical results (not shown here) at $f = 1.27$ GHz for varying $\bar{H} = \{10; 50; 100; 150\}$ cm lead to the same observations and conclusions. It is also seen that the polarization ratio is always equal to 1 for $\sigma_{r,1}$, and increases from 1 to more than 4 for $\sigma_{r,2}^{tot}$ for all frequencies.

[34] In Figure 12, the influence of the lower surface RMS slope σ_{sB} is studied at a fixed radar frequency $f = 1.27$ GHz, by taking $\sigma_{sB} = \{0.1; 0.2; 0.3; 0.4\}$. As expected, and as in Figure 8, increasing σ_{sB} induces a broadening of the second-order NRCS contribution $\sigma_{r,2}$ as well as of the total $\sigma_{r,2}^{tot}$.

[35] In Figure 13, the influence of the upper surface RMS slope σ_{sA} is studied at a fixed radar frequency $f = 1.27$ GHz, by taking $\sigma_{sA} = \{0.1; 0.2; 0.3\}$. This is then similar to Figure 9
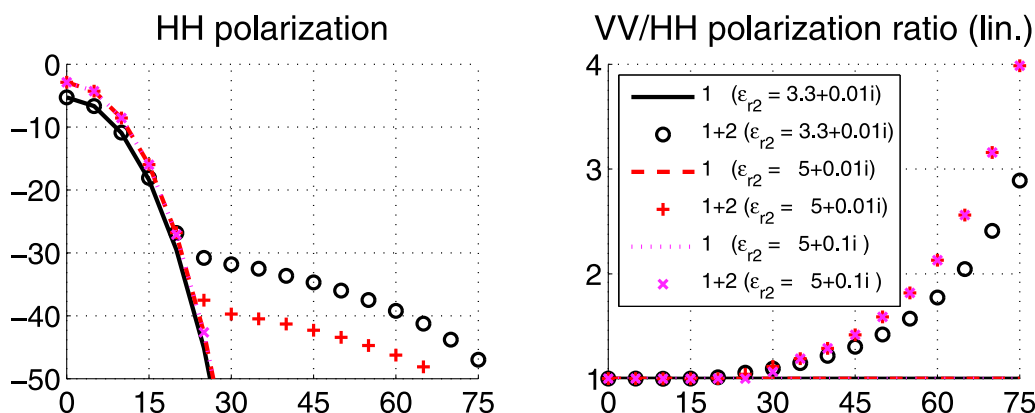
Figure 10. Same simulations as in Figure 7, but for various sand layer moisture, characterized by different relative permittivities $\epsilon_{r2} = \{3.3 + 0.01i; 5.0 + 0.01i; 5.0 + 0.1i\}$ with a constant layer thickness $\bar{H} = 30$ cm.
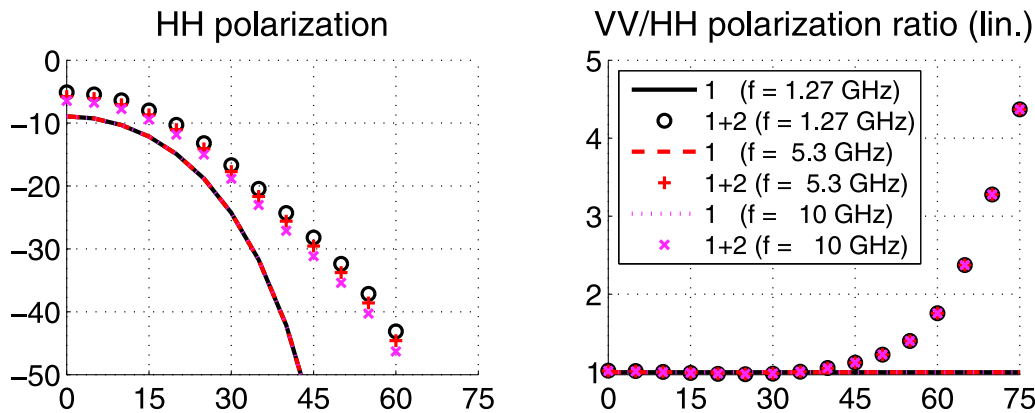
Figure 11. Monostatic plot of the NRCS of sand over hyper-saline clay soil (example of Lop Nur lake) with respect to the observation angle θ_r at three radar frequencies $f = 1.27$ GHz, $f = 5.3$ GHz, and $f = 10$ GHz.

for the first case. Increasing the upper RMS slope σ_{sA} induces a broadening of the monostatic NRCS $\sigma_{r,1}$: the near nadir ($\theta_r = 0$) monostatic NRCS decreases, but the decrease in $\sigma_{r,1}$ when θ_r increases is slower. The second-order contribution $\sigma_{r,2}$ is only slightly broadened when σ_{sA} increases. Then, near nadir, the sub-surface layer influence is larger because the difference between $\sigma_{r,1}$ and $\sigma_{r,2}^{tot}$ increases for increasing σ_{sA}. As in Figure 9, the polarization ratio of $\sigma_{r,2}^{tot}$ decreases for increasing σ_{sA}.

[36] The influence of the inner layer permittivity ϵ_{r2} is studied in Figure 14 for $f = 1.27$ GHz by taking $\epsilon_{r2} = \{4.43 + i0.01; 8 + i0.01; 8 + i0.05\}$. This is then similar to Figure 10 for the first case. Comparing the results for $\epsilon_{r2} = 8 + i0.01$ and $\epsilon_{r2} = 4.43 + i0.01$, the increase of the real part of ϵ_{r2} induces an increase of the first-order NRCS $\sigma_{r,1}$, and a slight decrease of $\sigma_{r,2}$ (and consequently of $\sigma_{r,2}^{tot}$) for low observation angles θ_r. Second, comparing the results for $\epsilon_{r2} = 8 + i0.01$ with those for $\epsilon_{r2} = 8 + i0.05$, increasing the imaginary part of ϵ_{r2} modifies $\sigma_{r,2}$ by increasing the propagation losses inside the sand layer, making the sub-surface layer's contributions smaller in the latter case.

### 3.5. Sensing Sand Soil Moisture Over Clay: Monostatic Case

[37] A last case is considered that corresponds to a dry sand layer overlying clay [*Kuo and Moghaddam*, 2007; *Moghaddam*

et al., 2007; *Kuo*, 2008]. The physical parameters are the same as in the work of *Kuo and Moghaddam* [2007]: the upper and lower interfaces have identical RMS heights $\sigma_{hA} = \sigma_{hB} = 3$ cm and correlation lengths $L_{cA} = L_{cB} = 50$ cm (which implies RMS slopes $\sigma_{sA} = \sigma_{sB} \simeq 0.085$ under the assumption of Gaussian surface statistics), and the layer thickness $\bar{H} = 30$ cm. For these surface statistics, the GO model should be applicable for $f \lesssim 2.5$ GHz. The influence of the moisture of the sand layer is studied at three radar frequencies: $f = 2.5$ GHz (S-band), $f = 5.3$ GHz (C-band), and $f = 10$ GHz (X-band). The model of *Peplinski et al.* [1995] was used to derive the soil relative permittivity, assuming a bulk density of 1.1 g/cm^3, a water temperature of 10°C, and a water salinity of 10 ppt (grams of salt per kg of water). Following *Kuo and Moghaddam* [2007], the sand layer is made up of 66% sand mass fraction and 10% clay mass fraction, and the clay layer is made up of 36% sand mass fraction and 40% clay mass fraction.

[38] Reference *Kuo and Moghaddam* [2007] considered backscattering versus incidence angle for this geometry at frequencies less than 1 GHz, at fixed soil moisture contents of 5% and 20% for the sand and clay layers, respectively. These parameters result in X-band relative permittivities of $4.1 + i0.55$ and $8.5 + i2.9$ for the sand and clay layers, so that the configuration is similar to that considered for sand over granite in Figures 7–9, although the lower interface RMS
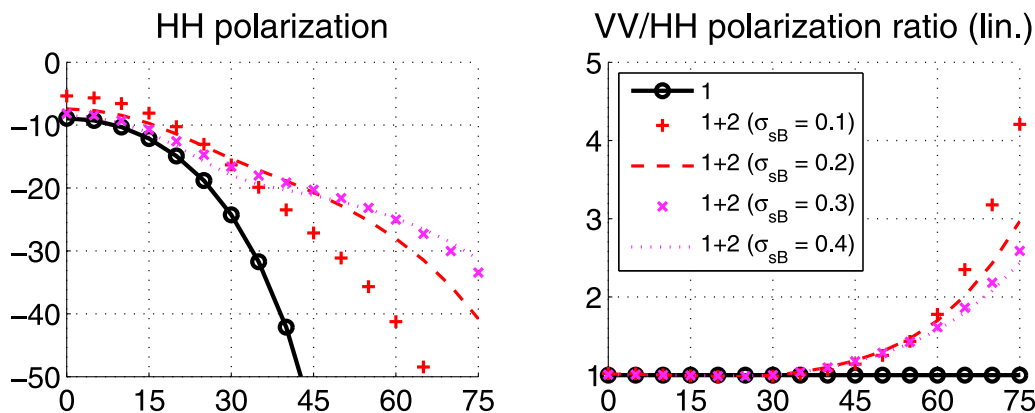
Figure 12. Same simulations as in Figure 11, but at a fixed radar frequency $f = 1.27$ GHz and various lower surface RMS slopes $\sigma_{sB} = \{0.1; 0.2; 0.3; 0.4\}$.
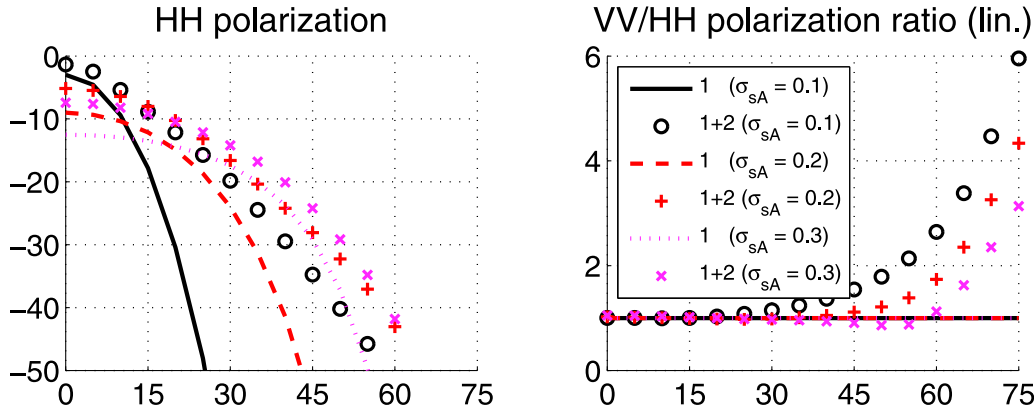
Figure 13. Same simulations as in Figure 11, but at a fixed radar frequency f = 1.27 GHz and various upper surface RMS slopes σ_{sA} = {0.1; 0.2; 0.3}.

slope is somewhat smaller than that in Figures 7 and 9. Monostatic plots versus incidence angle (not presented here) are therefore similar to those in Figures 7–9, except for a reduced broadening of the second-order NRCS $\sigma_{r,2}$. As a consequence, the subsurface layer contributes significantly to the total NRCS at smaller observation angles (down to $10 - 15°$, approximately), but the difference between $\sigma_{r,1}$ and $\sigma_{r,2}$ is reduced. Also $\sigma_{r,2}$ decreases more rapidly as θ_r increases, so that the lower layer's impact is not significant beyond incidence angles of approximately 35°.

[39] For a fixed incidence angle $\theta_i = 25°$, Figure 15 plots the monostatic NRCS as the sand layer moisture varies from 0 to 10%. The results show generally small backscattered returns for these smooth surfaces, but also that for the lower frequency f = 2.5 GHz, the total second-order NRCS $\sigma_{r,2}^{tot}$ is always larger than the first-order $\sigma_{r,1}$. Increasing the sand moisture increases both the real and imaginary parts of its relative permittivity: at f = 2.5 GHz, it increases from ϵ_{r2} = 2.41 + i0.028 for 0% moisture to ϵ_{r2} = 7.43 + i0.682 for 10% moisture (which must be compared to the lower clay layer relative permittivity: ϵ_{r3} = 11.11 + i1.688). As a consequence, the transmission coefficients through the upper interface decrease (and meanwhile, the reflection coefficient onto the upper interface increases) and the propagation losses inside the sand layer increase. Both these factors reduce subsurface contributions as the sand moisture

increases. It can be seen that as the real part of $n_2 = \sqrt{\epsilon_{r2}}$ increases only slightly compared to its imaginary part, the decrease of $\sigma_{r,2}$ is mainly due to the propagation losses. This is confirmed by the behavior of $\sigma_{r,1}$ which increases only slightly when the sand moisture increases.

[40] The same general observations and analyses can be made for the higher frequencies. The main difference comes from the fact that increasing the frequency implies a significant decrease of the amplitude of $n_3 = \sqrt{\epsilon_{r3}}$, and also a general significant increase of the imaginary part of $n_2 = \sqrt{\epsilon_{r2}}$ which implies additional attenuation of returns from the subsurface layer.

4. Conclusion

[41] In this paper, the GO-layer model, which was developed for calculating the NRCS of random rough layers [*Pinel et al.*, 2010], was extended to the calculation of the covariance of the scattered field between two polarizations *pq* and *rs*. This makes it possible to compute the correlation amplitude and phase, as well as other polarimetric features, such as entropy, anisotropy, mean alpha angle, etc. [*Cloude and Pottier*, 1996, 1997] not considered in this paper.

[42] Model predictions were examined for the remote sensing of (dry) sand over granite, with fully polarimetric NRCS and correlation plots shown in the complete bistatic
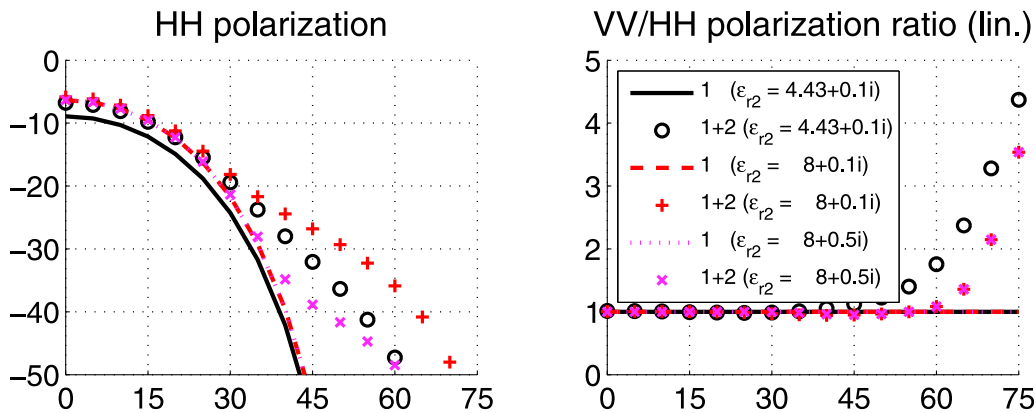
Figure 14. Same simulations as in Figure 11, but at a fixed radar frequency f = 1.27 GHz and various inner layer permittivities ϵ_{r2} = {4.43 + i0.01; 8 + i0.01; 8 + i0.05}.
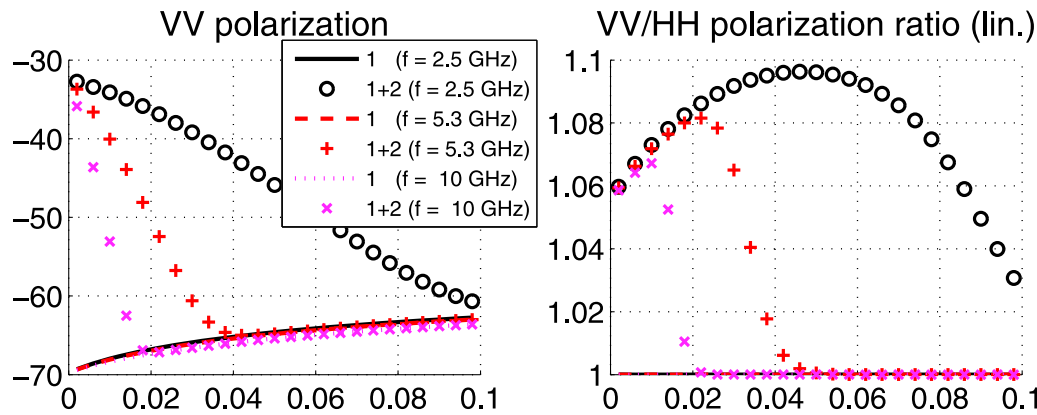
Figure 15. Plot of the monostatic NRCS of sand over clay with respect to the sand moisture at three radar frequencies $f = 2.5$ GHz, $f = 5.3$ GHz, and $f = 10$ GHz, for $\theta_i = 25°$.

scattering patterns. The results highlight significant differences between the single sand surface case and the rough layer case, suggesting that the presence of a subsurface layer and potentially its properties may be discernible in both NRCS and polarimetric quantities. In particular, near-specular portions of the bistatic pattern were determined where significant co-pol decorrelation occurred, as well as sub-surface layer visibility, suggesting potential applications in GNSS reflections sensing of sub-surface regions.

[43] Monostatic results were also presented for varying medium and surface parameters in order to study their influence. It was found that dielectric contrast and attenuation are important factors in the sensing of sub surface layers, but also that the roughness of both layers plays an important role in determining when the lower interface impacts the total observed cross section. The sand-over-granite plots presented can provide useful guidance for interpreting the influence of these factors in the remote sensing of arid regions. Monostatic predictions were also presented for the subsurface sensing of hyper-saline clay soil under sand (example of Lop Nur lake). Owing to a higher contrast of permittivities as well as a lower σ_{sB}, the lower clay soil had an increased effect on total returns. The impact of soil moisture on monostatic sensing situations involving sub-surface layers was also illustrated.

References

Berginc, G., and C. Bourrely (2007), The small-slope approximation method applied to a three-dimensional slab with rough boundaries, *Prog. Electromagn. Res.*, *73*, 131–211.

Cloude, S., and E. Pottier (1996), A review of target decomposition theorems in radar polarimetry, *IEEE Trans. Geosci. Remote Sens.*, *34*, 498–518.

Cloude, S., and E. Pottier (1997), An entropy based classification scheme for land applications of polarimetric SAR, *IEEE Trans. Geosci. Remote Sens.*, *35*, 68–78.

Demir, M. (2007), Perturbation theory of electromagnetic scattering from layered media with rough interfaces, Ph.D. thesis, Ohio State Univ., Columbus.

Duan, X., and M. Moghaddam (2010), Electromagnetic scattering from arbitrary random rough surfaces using stabilized extended boundary condition method (SEBCM) for remote sensing of soil moisture, in *Proceedings of IEEE International Geoscience and Remote Sensing Symposium*, p. 1386, IEEE Press, Piscataway, N. J.

Elachi, C., L. Roth, and G. Schaber (1984), Spaceborne radar subsurface imaging in hyperarid regions, *IEEE Trans. Geosci. Remote Sens.*, *GE-22*, 383–388.

Fuks, I. (1998), Radar contrast polarization dependence on subsurface sensing, in *Proceedings of IEEE International Geoscience and Remote Sensing Symposium*, vol. 3, pp. 1455–1459, IEEE Press, Piscataway, N. J.

Gong, H., Y. Shao, A. Cai, and C. Xie (2009a), Subsurface microwave remote sensing and scattering modelling on hyper-saline soil: Example of Lop Nur, in *Proceedings of IEEE International Geoscience and Remote Sensing Symposium*, vol. 3, IEEE Press, Piscataway, N. J.

Gong, H., Y. Shao, G. Wang, and A. Cai (2009b), Analysis and modeling about scattering mechanisms for the "Ear" feature of Lop Nur on SAR images, 18 pp.

Grandjean, G., P. Paillou, P. Dubois-Fernandez, T. August-Bernex, N. Baghdadi, and J. Achache (2001), Subsurface structures detection by combining L-band polarimetric SAR and GPR data: Example of the Pyla Dune (France), *IEEE Trans. Geosci. Remote Sens.*, *39*, 1245–1258.

Imperatore, P., A. Iodice, and D. Riccio (2010), Physical meaning of perturbative solutions for scattering from and through multilayered structures with rough interfaces, *IEEE Trans. Antennas Propag.*, *58*, 2710–2724.

Kuo, C. (2008), Full wave 2D modeling of scattering and inverse scattering for layered rough surfaces with buried objects, Ph.D. thesis, Univ. of Mich., Ann Arbor.

Kuo, C., and M. Moghaddam (2007), Electromagnetic scattering from multi-layer rough surfaces with arbitrary dielectric profiles for remote sensing of subsurface soil moisture, *IEEE Trans. Geosci. Remote Sens.*, *45*, 349–366.

Kuo, C.-H., and M. Moghaddam (2006), Scattering from multilayer rough surfaces based on the extended boundary condition method and truncated singular value decomposition, *IEEE Trans. Antennas Propag.*, *54*, 2917–2929.

Moghaddam, M., Y. Rahmat-Samii, E. Rodriguez, D. Entekhabi, J. Hoffman, D. Moller, L. Pierce, S. Saatchi, and M. Thomson (2007), Microwave observatory of subcanopy and subsurface (MOSS): A mission concept for global deep soil moisture observations, *IEEE Trans. Geosci. Remote Sens.*, *45*, 2630–2643.

Peplinski, N., F. Ulaby, and M. Dobson (1995), Dielectric properties of soils in the 0.3-1.3-Ghz range, *IEEE Trans. Geosci. Remote Sens.*, *33*, 803–807.

Pinel, N., and C. Bourlier (2008), Scattering from very rough layers under the geometric optics approximation: Further investigation, *J. Opt. Soc. Am. A*, *25*, 1293–1306.

Pinel, N., N. Déchamps, C. Bourlier, and J. Saillard (2007), Bistatic scattering from one-dimensional random rough homogeneous layers in the high-frequency limit with shadowing effect, *Waves Random Complex Media*, *17*, 283–303.

Pinel, N., J. Johnson, and C. Bourlier (2009), A geometrical optics model of three dimensional scattering from a rough surface over a planar surface, *IEEE Trans. Antennas Propag.*, *57*, 546–554.

Pinel, N., J. Johnson, and C. Bourlier (2010), A geometrical optics model of three dimensional scattering from a rough layer with two rough surfaces, *IEEE Trans. Antennas Propag.*, *58*, 809–816.

Prigent, C., J. Munier, B. Thomas, and G. Ruffié (2005), Microwave signatures over carbonate sedimentary platforms in arid areas: Potential geological applications of passive microwave observations?, *Geophys. Res. Lett.*, *32*, L23405, doi:10.1029/2005GL024691.

Saillard, M., and G. Toso (1997), Electromagnetic scattering from bounded or infinite subsurface bodies, *Radio Sci.*, *32*, 1347–1360.

RS0E20

PINEL ET AL.: ROUGH LAYERS POLARIMETRIC SCATTERING

RS0E20

Sarabandi, K., and T. Chiu (1997), Electromagnetic scattering from slightly rough surfaces with inhomogeneous dielectric profiles, *IEEE Trans. Antennas Propag.*, *45*, 1419–1430.

Shao, Y., H. Gong, C. Xie, and A. Cai (2009), Detection subsurface hyper-saline soil in Lop Nur using full-polarimetric SAR data, in *Proceedings of IEEE International Geoscience and Remote Sensing Symposium*, vol. 3, IEEE Press, Piscataway, N. J.

Tabatabaeenejad, A., and M. Moghaddam (2006), Bistatic scattering from three-dimensional layered rough surfaces, *IEEE Trans. Geosci. Remote Sens.*, *44*, 2102–2114.

Yarovoy, A., R. de Jongh, and L. Ligthart (2000), Scattering properties of a statistically rough interface inside a multilayered medium, *Radio Sci.*, *35*, 455–462.

Zavorotny, V. U., K. M. Larson, J. J. Braun, E. E. Small, E. D. Gutman, and A. L. Bilich (2010), A physical model for GPS multipath caused by land reflections: Toward bare soil moisture retrievals, *IEEE J. Selec. Top. Appl. Earth Obs. Remote Sens.*, *3*, 1404–1939.

C. Bourlier and N. Pinel, Lunam Université - Université de Nantes, UMR CNRS 6164 Institut d'Electronique et de Télécommunications de Rennes, Polytech Nantes La Chantrerie, rue C. Pauc, BP 50609, F-44306 Nantes CEDEX 3, France. (christophe.bourlier@univ-nantes.fr; nicolas.pinel@univ-nantes.fr)

J. T. Johnson, Department of Electrical and Computer Engineering, Ohio State University, Columbus, OH 43210, USA. (johnson@ece.osu.edu)